Structural, elastic, electronic, optical and thermoelectric properties of the Zintl-phase Ae$_3$AlAs$_3$ (Ae = Sr, Ba)

A. Benahmed, A. Bouhemadou, B. Alqarni, N. Guechi, Y. Al-Douri, R. Khenata & S. Bin-Omran

📅 Published online: 19 Jan 2018.

✎ Submit your article to this journal ⫯

🔍 View related articles ⫯

⬚ View Crossmark data ⫯

Taylor & Francis
Taylor & Francis Group

Check for updates

Structural, elastic, electronic, optical and thermoelectric properties of the Zintl-phase Ae_3AlAs_3 (Ae = Sr, Ba)

A. Benahmed[a], A. Bouhemadou[a], B. Alqarni[b], N. Guechi[c], Y. Al-Douri[d,e] (iD),
R. Khenata[f] and S. Bin-Omran[b]

[a]Laboratory for Developing New Materials and their Characterization, University of Setif 1, Setif,
Algeria; [b]Department of Physics and Astronomy, College of Science, King Saud University, Riyadh, Saudi
Arabia; [c]Faculty of Science, Department of Science of Matter, University of Medea, Medea, Algeria;
[d]Nanotechnology and Catalysis Research Center (NANOCAT), University of Malaya, Kuala Lumpur,
Malaysia; [e]Faculty of Science, Physics Department, University of Sidi-Bel-Abbes, Algeria; [f]Laboratoire de
Physique Quantique de la Matière et de Modélisation Mathématique (LPQ3 M), Université de Mascara,
Mascara, Algeria

ABSTRACT

First-principles calculations were performed to investigate
the structural, elastic, electronic, optical and thermoelectric
properties of the Zintl-phase Ae_3AlAs_3 (Ae = Sr, Ba) using two
complementary approaches based on density functional
theory. The pseudopotential plane-wave method was used
to explore the structural and elastic properties whereas the
full-potential linearised augmented plane wave approach
was used to study the structural, electronic, optical and
thermoelectric properties. The calculated structural
parameters are in good consistency with the corresponding
measured ones. The single-crystal and polycrystalline
elastic constants and related properties were examined in
details. The electronic properties, including energy band
dispersions, density of states and charge-carrier effective
masses, were computed using Tran-Blaha modified Becke-
Johnson functional for the exchange-correlation potential. It
is found that both studied compounds are direct band gap
semiconductors. Frequency-dependence of the linear optical
functions were predicted for a wide photon energy range
up to 15 eV. Charge carrier concentration and temperature
dependences of the basic parameters of the thermoelectric
properties were explored using the semi-classical Boltzmann
transport model. Our calculations unveil that the studied
compounds are characterised by a high thermopower for both
carriers, especially the p-type conduction is more favourable.

1. Introduction

Thermoelectric (TE) materials play an important role in global sustainable energy
solution. These materials are investigated not only owing to their high potential

---

CONTACT A. Bouhemadou ✉ a_bouhemadou@yahoo.fr, abdelmadjid_bouhemadou@univ-setif.dz

of converting directly waste thermal energy to useful electrical energy but also to their capability to reduce effectively the environmental pollution. The ability of a TE material to convert heat directly into electricity is controlled by the dimensionless parameter ZT [1,2], the so-called figure of merit, which is given by $ZT = \frac{S^2\sigma}{\kappa}T$, where S is the Seebeck coefficient (thermopower), σ is the electrical conductivity, κ is the thermal conductivity and T is the absolute temperature. A promising TE material should have a large ZT value. From its expression, it is very clear that a high ZT, requires a large thermopower S, high electrical conductivity σ and a low thermal conductivity κ, i.e. an ideal thermoelectric material must strike a balance between these conflicting requirements. However, due to the strongly coupled nature between S, σ and the electronic component of the thermal conductivity κ, it is difficult for a material to have simultaneously high S, high σ and low κ. A high Seebeck coefficient is attained in a low charge-carrier concentration, while a large electrical conductivity is attained in a high charge-carrier concentration; S and σ have an opposite dependence on charge-carrier concentration, so a balance between S and σ must be achieved through a chemical doping [1,3]. Therefore, obtaining a TE material with a high ZT value is a challenging task.

Currently, many kinds of thermoelectric materials have been widely studied, such as Zintl-phases, nanostructured compounds, zinc antimonides, oxides, half-Heusler compounds, clathrates and skutterudites [4–12]. Zintl-phases, a broad class of intermetallic compounds characterised by cations that donate their electrons to support the formation of covalency bonded anionic substrates, have emerged as a promising class of materials for thermoelectric applications due to their complex crystal structures, interesting electronic, chemical and physical properties [13,14]. The structural requirements of Zintl-phases are explained by assuming the presence of both anionic networks and electropositive cations [13]. The anionic networks are covalent and the cationic part is ionic in nature. The resulting mix of ionic and covalent bonds frequently leads to complex crystal structures with large unit cells; such a complex crystal can enable them to have low thermal conductivity [15–17]. Additionally, the Zintl-phase chemistry suggests that the fundamental transport parameters can be modified by doping to achieve a good balance between S and σ, consequently thus can lead to a high power factor [18,19]. Therefore, Zintl-phases provide desired characteristics for high ZT and improved thermoelectric performance since their thermal conductivities are intrinsically low. This has been demonstrated in several previous studies, including Ca_3AlSb_3 [20], $Ca_5Al_2Sb_6$ [21] and $Ca_5Ga_2As_6$ [22]. This further actuates us to search for other possible new Zintl-phase materials for suitable TE candidates. In the current study, we are interested in investigating the Ae_3AlAs_3 (Ae = Sr, Ba) compounds that were recently synthesised [23]. These compounds crystalise in the Ba_3AlSb_3 structure type with the space group $Cmce$. The structural properties of the title compounds, including the lattice parameters and atomic position coordinates, have been investigated using single-crystal $X\text{-}ray$ diffraction. The

band structure and density of states of Ba_3AlAs_3 have been carried out using the tight-binding linear muffin-tin orbital (TB-LMTO) method [23]. To the best of our knowledge, some basic physical properties, such as elastic, optical and thermoelectric properties of these newly synthesised compounds are not studied. Therefore, the main object of the present study is the investigation of the structural, elastic, electronic, optical and thermoelectric properties of the Ae_3AlAs_3 (Ae = Sr, Ba) compounds. The structure of the present paper is as follows: Section 2 describes briefly the computation setting. Section 3 reports and discusses the obtained results, with subsections dedicated to structural, elastic, electronic, optical and thermoelectric properties. The paper is finished with a general conclusion.

2. Computational details

First-principles calculations were performed by employing two complementary methods based on density functional theory. The elastic properties were evaluated using the pseudopotential plane wave (PP-PW) method as implemented in the CASTEP code [24], while the electronic and optical properties were carried out using the full potential linearised augmented plane wave method (FP-LAPW) as incorporated in the WIEN2 k suite of programs [25]. The structural properties were evaluated using both the aforementioned methods. The structural data from Ref. [23] were taken as initial input for our calculations.

For the pseudopotential plane wave approach, Vanderbilt ultra-soft pseudopotentials [26] were used to describe the interactions between core and valence electrons of each atom. The Ba: $5s^25p^66s^2$, Sr: $4s^24p^65s^2$, Al: $3s^23p^1$ and As: $4s^24p^3$ states were treated as valence electrons. The electronic exchange and correlation effects were treated through the generalised gradient approximation functional in the version of Perdew et al. [27], the so-called GGA-PBEsol. The plane-wave basis set energy cut-off was set at 350 eV. The Brillouin zone integration was replaced by a summation over a $6 \times 6 \times 3$ k-point mesh generated according to Monkhorst-Pack scheme [28]. This set of parameters assures a total energy tolerance of 1×10^{-5} eV/atom, a maximum force tolerance of 0.01 eV/Å, a maximum stress of 0.02 GPa and a maximum displacement of 5.0×10^{-4} Å}.

It is well known that the first-principles methods with the common generalised gradient approximation (GGA) yield good values for the ground state structures but they underestimate the band gaps of semiconductors and insulators typically by 30–50% [29–31] when compared to experiments. The underestimation of the band gaps of semiconductors and isolators when using GGA is because this approximation cannot describe exactly the exchange–correlation potential. Some sophisticated approaches, such as the weighted density approximation (WDA) [32], the GW approximation [33] and the Tran-Blaha modified Becke-Johnson (TB-mBJ) potential [34], have been developed in order to overcome this insufficiency and to obtain reliable band gap values for semiconductors and insulators

compared to the measured ones. The TB-mBJ is computationally cheaper than the other aforementioned methods and produces energy band gaps almost comparable with the corresponding measured ones with a reasonable computation time. Therefore, in addition to the GGA-PBEsol, the electronic, optical and thermoelectric properties of the investigated compounds were calculated using the TB-mBJ functional as implemented in the WIEN2 k package [25]. The WIEN2 k code is an implementation of the full-potential linearised augmented plane wave (FP-LAPW). In the FP-LAPW method, the unit cell is divided into non-overlapping spheres centred at the atomic sites (labelled muffin-tin spheres (MTS)) and the space between the MTS (labelled interstitial region (IR)). A linear combination of radial atomic functions time spherical harmonics is used inside the MTS to expand the wave functions, whereas a plane wave basis set is used in the IR. In order to achieve the energy convergence of the eigenvalues, the wave functions in the interstitial regions were expanded in plane waves with a cut-off parameter $K_{Max} = 4\ (a.u.)^{-1}$. The Brillouin zone integration was replaced by a $6 \times 6 \times 3$ k-point mesh. The iteration process was repeated until the calculated total energy of the crystal converged to less than 10^{-5} Ry. The muffin-tin radii were selected as 2.35 $a.u.$ for Sr, 2.40 $a.u.$ for Ba, 2.18 $a.u.$ for Al and 2.44 $a.u.$ for As.

3. Results and discussion

3.1. Structural parameters

Single-crystal *X-ray* diffraction technique reveals that the Ae_3AlAs_3 (Ae = Sr, Ba) compounds crystallise in the orthorhombic Ba_3AlSb_3-type structure, space group *Cmce*, with eight formula units in one unit cell [23] (Figure 1). There are two kinds of Ae ($Ae1$ and $Ae2$) and As (As1 and As2) atoms. The Wyckoff atomic positions in the Ae_3AlAs_3 unit cell are $Ae1$: $8f$ $(0, y_{Ae1}, z_{Ae1})$; $Ae2$: $16\,g$ $(x_{Ae2}, y_{Ae2}, z_{Ae2})$; Al: $8d$ $(x_{Al}, 0, 0)$; As1: $8f$ $(0, y_{As1}, z_{As1})$ and As2: $16\,g$ $(x_{As2}, y_{As2}, z_{As2})$. The fully optimised crystal structure, including lattice parameters and atomic positions, for the orthorhombic Sr_3AlAs_3 and Ba_3AlAs_3 crystals, using both the PP-PW and FP-LAPW methods, are collected in Tables 1 and 2 in comparison with experimental findings. The inspection of Table 1 data indicates a good agreement between the calculated values for the lattice parameters (a, b and c) and the corresponding measured ones. Using the PP-PW (FP-LAPW) method, the deviations between the theoretical values of a, b and c and the corresponding experimental ones do not exceed +2.03% (−0.51%), −0.72% (−3.27) and +0.67% (−0.01%), respectively, in Sr_3AlAs_3, and −0.03% (−1.38%), −0.34% (−7.48%) and −0.107% (−0.51%), respectively, in Ba_3AlAs_3. Table 2 data show also a very good agreement between the calculated atomic position coordinates (x, y, z) and the corresponding measured ones, indicating the reliability of the performed calculations.
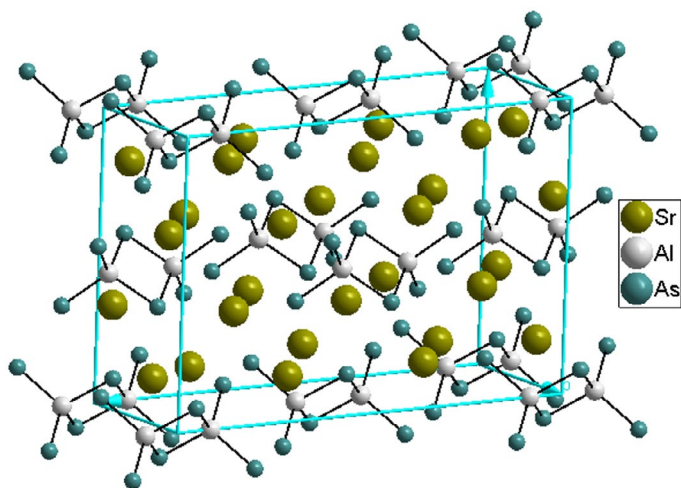
Figure 1. (colour online) One unit cell of Sr$_3$AlAs$_3$.

Table 1. Calculated lattice parameters (a, b and c, in Å) and unit-cell volume (V, in Å^3) for the Sr$_3$AlAs$_3$ and Ba$_3$AlAs$_3$ compounds, compared with the available experimental data.

	a	b	c	V
Sr$_3$AlAs$_3$				
Present work[a]	19.0503	6.3501	12.7002	1587.22
Present work[b]	19.5368	6.5174	12.7729	1626.39
Expt. [23]	19.149	6.5652	12.6871	1595.0
Ba$_3$AlAs$_3$				
Present work[a]	19.5795	6.3501	13.2294	1737.92
Present work[b]	19.8475	6.8406	13.2741	1802.22
Expt. [23]	19.854	6.8636	13.3589	1810.3

[a]Using FP-LAPW method within GGA-PBEsol.
[b]Using PP-PW method within GGA-PBEsol.

Table 2. Atomic position coordinates for the Sr$_3$AlAs$_3$ and Ba$_3$AlAs$_3$ compounds, compared with the available experimental data.

	x			y			z		
Atom	Present [a]	Present [b]	Expt. [c]	Present [a]	Present [b]	Expt. [c]	Present [a]	Present [b]	Expt. [c]
Sr$_3$AlAs$_3$									
Sr1	0	0	0	0.17601	0.17924	0.17463	0.34919	0.34707	0.34891
Sr2	0.17701	0.17755	0.17691	0.31155	0.30838	0.31222	0.13114	0.13009	0.13126
Al	0.08477	0.08377	0.08500	0	0	0	0	0	0
As1	0	0	0	0.21042	0.21277	0.20879	0.10330	0.10079	0.10250
As2	0.34107	0.34207	0.34135	0.29518	0.29326	0.29606	0.12081	0.11794	0.12022
Ba$_3$AlAs$_3$									
Ba1	0	0	0	0.17027	0.17109	0.17015	0.34671	0.34766	0.34685
Ba2	0.17572	0.17535	0.17563	0.31309	0.31201	0.31318	0.13024	0.12975	0.13014
Al	0	0.08316	0.08294	0	0	0	0	0	0
As1	0	0	0	0.20320	0.20566	0.20319	0.09628	0.09791	0.09613
As2	0.34335	0.34294	0.34345	0.30899	0.30728	0.30905	0.11818	0.11954	0.11805

[a]Using the FP-LAPW method within the GGA-PBEsol.
[b]Using the PP-PW method within the GGA-PBEsol.
[c]Ref. [23].

Table 3. Calculated elastic constants (C_{ij}, in GPa) for the Ae_3AlAs_3 (Ae = Sr, Ba) compounds.

System	C_{11}	C_{22}	C_{33}	C_{44}	C_{55}	C_{66}	C_{12}	C_{13}	C_{23}
Sr_3AlAs_3	61.7	74.6	76.6	32.4	28.6	30.3	27.1	22.6	31.3
Ba_3AlAs_3	80.2	71.1	81.5	17.1	4.7	14.1	21.6	15.3	24.0

3.2. Elastic constants and related properties

Accurate calculations of the elastic constants C_{ij} are very helpful to understand many physical properties of solids. The elastic constants C_{ij} provide valuable information on the stability and stiffness of crystals against externally applied strain, bonding characteristics, specific heat, thermal expansion, Debye temperature, Grüneisen parameter and so on [35–37]. In general, the elastic behaviour of a completely asymmetric material is specified by 21 independent elastic constants C_{ij} but due to the presence of some symmetries, this number can be reduced. Only nine independent elastic constants, namely C_{11}, C_{22}, C_{33}, C_{44}, C_{55}, C_{66}, C_{12}, C_{13} and C_{23}, are required to characterise the elastic properties of an orthorhombic crystal. The elastic constants C_{ij} were evaluated via the calculation of three stress tensors corresponding to three different deformation patterns applied to the equilibrium lattice. The calculated elastic constants C_{ij} using the strain–stress method [24] for the title compounds are reported in Table 3. There are no theoretical or experimental results for the elastic constants C_{ij} in the scientific literature to be compared with the present results. Then, our results can serve as a prediction for future investigations.

The elastic constants C_{11}, C_{22} and C_{33} reflect the resistance to the linear compression along the [100], [010] and [001] crystallographic directions, respectively. From Table 3, one can note that the values of the three aforementioned elastic constants are not remarkably different, suggesting that the resistance to the compression deformation along the [100], [010] and [001] directions are approximately equal. The values of C_{11}, C_{22} and C_{33} are higher than those of the other elastic constants C_{ij}, demonstrating that the resistance of the two studied compounds to the shear distortion is lower than their resistance against the compressional deformation.

The mechanical stability of crystals leads to some restrictions on their elastic constants. For orthorhombic crystals, these mechanical stability criteria are [38]:

$$C_{11} + C_{22} - 2C_{12} > 0, \ C_{11} + C_{33} - 2C_{13} > 0, \ C_{22} + C_{33} - 2C_{23} > 0, \ C_{11} > 0, \ C_{22} > 0,$$
$$C_{33} > 0, \ C_{44} > 0, \ C_{55} > 0, \ C_{66} > 0, \ C_{11} + C_{22} + C_{33} + 2C_{12} + 2C_{13} + 2C_{23} > 0$$

The calculated elastic constants of the two studied compounds (Table 3) satisfy the aforementioned criteria. This indicates that these compounds are mechanically stable.

It is not possible to measure the individual elastic constants C_{ij} when single-crystal samples cannot be obtained. In this case, polycrystalline elastic moduli, such as the bulk modulus B and the shear modulus G, can be measured. Theoretically,

we can deduce the polycrystalline (aggregates of single-crystals with random orientations) elastic moduli, which are more desirable for technological characterisation of materials, from the calculated single-crystal elastic constants C_{ij}. The isotropic shear and bulk moduli (G and B) can be calculated from the anisotropic single-crystal elastic constants C_{ij} using the Hill approximation [39], which takes the arithmetic average of the Voigt [40] and Reuss [41] approximations. The Voigt approach determines the upper limit of the actual effective moduli, while the Reuss approach determines the lower limit of these parameters. The expression of the Voigt bulk and shear moduli (B_V and G_V) and the Reuss bulk and shear moduli (B_R and G_R) can be found in Ref. [42]. The Young's modulus E and Poisson's ratio σ can be obtained from B and G using the well-known relationships [43,44]. The calculated values of the aforementioned elastic moduli are given in Table 4. The obtained results allow us to make the following conclusions:

(i)   Due to the low value of the bulk modulus, which represents the resistance to volume change by external applied pressure, one can conclude that the considered materials are characterised by a weak resistance to the volume change; i.e. by a high compressibility. The lower value of the shear modulus, which characterises the resistance to shear deformation, demonstrates that Ba_3AlAs_3 and Sr_3AlAs_3 have also a weak resistance to shape change. Besides, the bulk modulus B is larger than the shear modulus G in both considered compounds, indicating a better capability of resistance to volume change than to shape change.

(ii) The Young's modulus E, defined as the ratio of linear stress to linear strain, can be used to provide a measure of the stiffness of a material. It is found that E of the two studied compounds is weak, indicating that these compounds will show a rather small stiffness. The results also demonstrate that Sr_3AlAs_3 is stiffer than Ba_3AlAs_3 in terms of B, G and E moduli.

(iii) The most widely used criterion to distinguish between ductile and brittle materials is the Pugh's one (B/G ratio) [45]. According to this criterion, a material can be classified as ductile if the B/G ratio is greater than 1.75; otherwise, it demonstrates brittleness. The obtained data foretell that Sr_3AlAs_3 ($B/G = 1.55$) should behaves as brittle material, while Ba_3AlAs_3 should demonstrates ductility. The classical criteria of Cauchy pressure can also be used to examine the brittle/ductile

Table 4. Calculated Reuss, Voigt and Hill bulk (B_R, B_V and B_H, in GPa) and shear (G_R, G_V and G_H, in GPa) moduli, Young's modulus (E, in GPa) and Poisson's ratio (σ, dimensionless) for isotropic polycrystalline Ae_3AlAs_3 ($Ae = Sr$, Ba) aggregates.

System	B_V	G_V	B_R	G_R	B_H	G_H	E_j			E	σ
							E_x	E_x	E_x		
Sr_3AlAs_3	41.65	39.60	40.92	26.15	41.29	26.60	72.80	60.30	72.52	65.70	0.23
Ba_3AlAs_3	39.41	32.73	39.39	12.02	39.40	15.32	72.80	60.30	72.52	40.69	0.32

character of materials [46]. Pettifor [47] indicated that Cauchy pressure can be adopted to capture the nature of the bonding. Materials with a positive Cauchy pressure possess metallic like bonds, thereby holding ductile characteristics. On the other hand, brittle materials would hold a negative Cauchy pressure. In orthorhombic materials, the Cauchy pressure in the three lattice directions can be expressed as follows [48]:$P_a^{Cauchy} = C_{22} - C_{44}$, $P_b^{Cauchy} = C_{13} - C_{55}$ and $P_c^{Cauchy} = C_{12} - C_{66}$. Based on the calculated single-crystal C_{ij} (Table 3), $P_a^{Cauchy} = -1.10\,GPa\,(6.90\,GPa)$, $P_b^{Cauchy} = -6.0\,GPa\,(10.60\,GPa)$ and $P_c^{Cauchy} = -3.0\,GPa\,(7.50\,GPa)$ for Sr_3AlAs_3 (Ba_3AlAs_3). These results confirm the brittleness of Sr_3AlAs_3 and ductility of Ba_3AlAs_3.

From the computed bulk and shear moduli, we can evaluate the longitudinal (V_l), transverse (V_t) and average (V_m) sound wave velocities in a polycrystalline material through the following relationships [49]:

$$V_l = \sqrt{(B_H + 4G_H/3)/\rho};\ V_t = \sqrt{G_H/\rho};\ V_m = \left[(2/V_t^3 + 1/V_l^3)/3\right]^{-1/3}$$

Debye temperature θ_D, which is associated with the lattice vibration, elastic constants, specific heat and melting point, can be predicated via the following common relation [49]:

$$\theta_D = \frac{h}{k_B}\left[\frac{3n}{4\pi}\left(\frac{N_A\rho}{M}\right)\right]^{\frac{1}{3}}V_m$$

Here, h and k_B are the constants of Planck and Boltzmann, respectively, n is the number of atoms per one formula unit, N_A is Avogadro's number, ρ denotes the mass density, M is the molecular mass. The calculated values of ρ, V_l, V_t, V_m and θ_D for the Ae_3AlAs_3 (Ae = Sr, Ba) compounds are collected in Table 5. Sr_3AlAs_3 has a larger Debye temperature than Ba_3AlAs_3; this is a predicted result because the bulk modulus of Sr_3AlAs_3 is somewhat larger than that of Ba_3AlAs_3. Up to now, there are no available data for these parameters in the scientific literature to be compared with our present findings.

An isotropic material displays the same physical properties irrespective of the direction in which those properties are measured. In general, the elastic response of a single-crystal is seldom isotropic; almost all the known crystals are elastically anisotropic, so their elastic moduli depend on the orientation of the applied force

Table 5. Calculated mass density (ρ), longitudinal, transverse and average sound velocities (V_l, V_t and V_m, in m/s unit) and Debye temperatures (θ_D, in K unit) for the Ae_3AlAs_3 (Ae = Sr, Ba) polycrystals.

System	ρ	V_l	V_t	V_m	θ_D
Sr_3AlAs_3	4.2033	4273.50	2331.94	2600.81	251.95
Ba_3AlAs_3	4.8925	3961.10	1769.79	1996.65	186.91

in respect of the crystallographic axes. The description of elastic anisotropy in materials is important because it influences various physical properties, such as unusual phonon modes, phase transformations, precipitation, dislocation dynamics, anisotropic plastic deformation, anomalous bcc slip, mechanical yield points, crack behaviour, elastic instability and internal friction [50]. The anisotropy in mechanical properties might be estimated using various anisotropy indexes and factors [51–56]. An even detailed picture of the elastic anisotropy can be emerged by plotting a three-dimensional surface representation showing the variation of the Young's modulus with the crystallographic directions. This directional dependence of the Young's modulus E for an orthorhombic crystal in an arbitrary direction is defined as [57]:

$$E = \left[S_{11}l_1^4 + 2S_{12}l_1^2l_2^2 + S_{22}l_2^4 + 2S_{23}l_2^2l_3^2 + S_{33}l_3^4 + 2S_{13}l_1^2l_3^2 + S_{44}l_2^2l_3^2 + S_{55}l_1^2l_3^2 + S_{66}l_1^2l_2^2 \right]^{-1}$$

Here, l_1, l_2 and l_3 are the direction cosines, which determine the angles between the axes a, b and c, respectively, and a given direction, and S_{ij} is the elastic compliance constants, which can be acquired from the inverse of the matrix of elastic constants. The distance from the origin of the coordinate system to this surface is equal to the Young's modulus in a given direction. For a perfectly isotropic medium, this surface would be a sphere, while the deviation of this surface from the spherical shape indicates the presence of a certain degree of elastic anisotropy. Figure 2 illustrates the directional dependence of the Young's modulus of the Sr_3AlAs_3 and Ba_3AlAs_3 compounds. Figure 1 shows that the degree of elastic anisotropy of Ba_3AlAs_3 is much more appreciable than that of Sr_3AlAs_3. A deeper look into the peculiar features of elastic anisotropy can be gauged by plotting the cross-section of the closed surface of E in the principal planes. For isotropic crystal, the plane projection curves are circular. From the cross sections plotted separately in Figure 1, we can see that there is a clear deviation from circular shape.

3.3. Electronic properties

3.3.1. Band structure

The electronic energy band dispersions along the high-symmetry directions in the Brillouin zone (BZ) for the Sr_3AlAs_3 and Ba_3AlAs_3 compounds, performed at the optimised structural parameters, using the FP-LAPW method with both the GGA-PBEsol and TP-mBJ approaches, are depicted in Figure 3. The Γ, Z, T, Y, S and R letters indicate the high symmetry points in the BZ of the Ae_3AlAs_3 (Ae = Sr, Ba) compounds and their coordinates are respectively (0,0,0), (0,0,0.5), (−0.5,0.5,0.5), (−0.5, 0.5, 0), (0,0.5,0) and (0,0.5,0.5) in the unit vectors of the reciprocal lattice. From Figure 2, one can note that Sr_3AlAs_3 has a direct band gap; the top of the valence band (VB) and the bottom of the conduction band (CB) are located at the Γ-point, while Ba_3AlAs_3 has an indirect band gap; the top
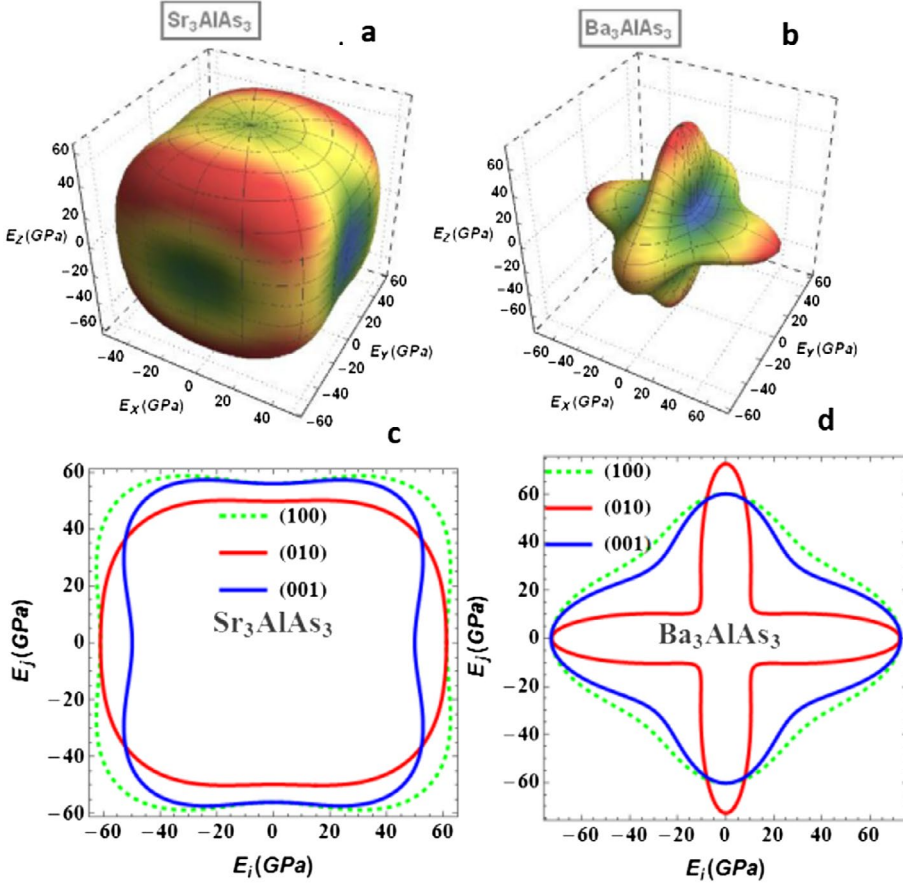
**Figure 2.** (colour online) 3D-directional dependence of the Young's modulus (*E*, in GPa) and its projection on the *ab*- {(001)}, *ac*- {(010)} and *ab*- {(100)} planes for the Sr$_3$AlAs$_3$ and Ba$_3$AlAs$_3$ compounds.

of the VB is located at the *Y*-point and the bottom of the CB is at the *Γ*-point. The calculated band structures using the TB-mBJ and GGA-PBEsol functionals have practically same features except the band gap values that are disparate. The calculated Sr$_3$AlAs$_3$ (Ba$_3$AlAs$_3$) energy band gap is 1.51 eV (1.28 eV) when using the TB-mBJ formalism, and is 0.90 eV (0.61 eV) when using the GGA-PBEsol. We note that the GGA and LDA functionals usually underestimate the energy band gap by 30–50% [30–32]. Therefore, one can appreciate that the TB-mBJ considerably improves the band gap values. There are no experimental values for the gaps of the studied compounds. The GGA-PBEsol band gap value for Ba$_3$AlAs$_3$ is in good agreement with the one predicted by Stanislav et al. [24] using the tight-binding linear muffin tin orbital (TB-LMTO) method within the LDA.

3.3.2. Density of states

Assignment of the electronic states compositing the electronic energy bands of the considered systems can be made with the help of the total and atomic decomposed
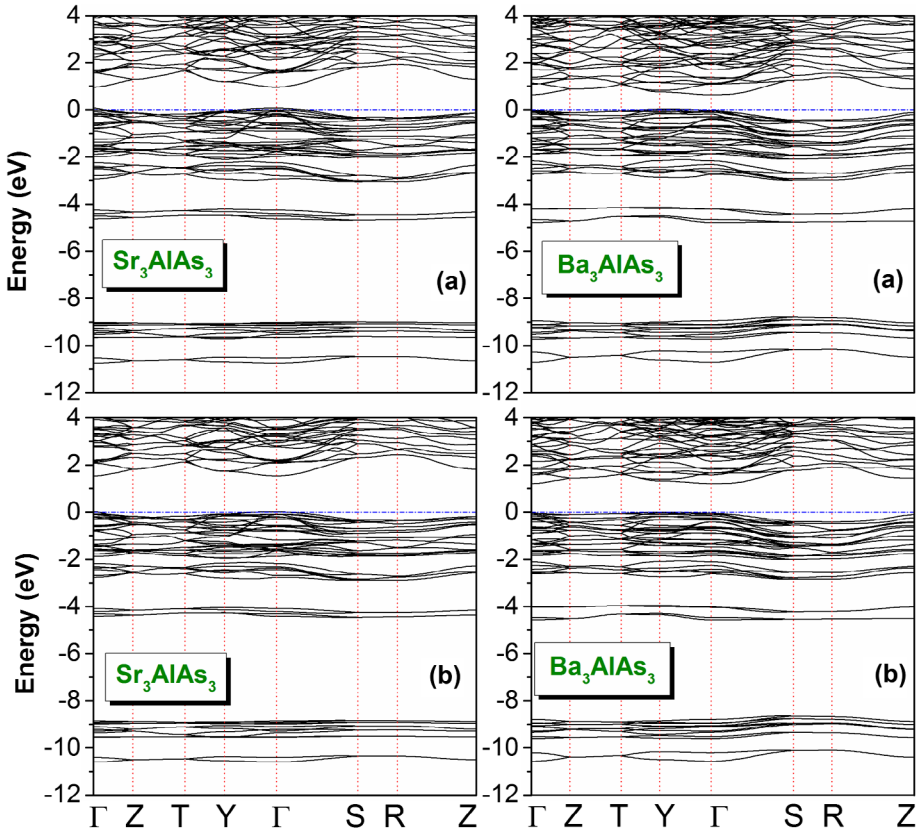
Figure 3. (colour online) Electronic band dispersion curves along some high symmetry directions in the Brillouin zone for the Ae_3AlAs$_3$ (Ae = Sr, Ba) compounds using the GGA-PBEsol (a) and the TB-mBJ (b) functionals.

partial densities of states (TDOS and PDOS) diagrams, which are shown in Figure 4. The Sr$_3$AlAs$_3$ and Ba$_3$AlAs$_3$ valence bands located in the energy range from −12 eV up to Fermi level (E_F) can be separated into four groups that are labelled V1, V2, V3 and V4 in the figure. For Sr$_3$AlAs$_3$, the lowest energy group V1, which is stretched from approximately −10.6 to −9.9 eV, is mainly formed of the As1-4s and As2-4s states. The second group V2, which spreads approximately from −9.7 to −8.5 eV, is mainly due to the As1-4p and Al-3s states with a very small contribution from an admixture of the Al-3s, Al-3p, Sr1-4p and Sr2-4p orbitals. The third group V3, located in the energy range from −4.6 to −3.97 eV, is mainly due to the As1-4p and Al-3s states. The fourth valence band group V4, which lays approximately from −3.0 eV up to Fermi level (E_F), is completely dominated by the As1-4p and As2-4p states with a small contribution from the Al-3p, Sr1-4s, Sr2-4s, Sr1-4p, Sr2-4p, Sr1-3d and Sr2-3d states. The bottom of the conduction band (C1) comes from the Sr1-3d and Sr2-3d states with a small contribution from the Al-3p and Al-3s states. For the Ba$_3$AlAs$_3$ compound, the V1 valence band group, from −10.7 to −9.97 eV, is mainly occupied by the As1-4s states with a small
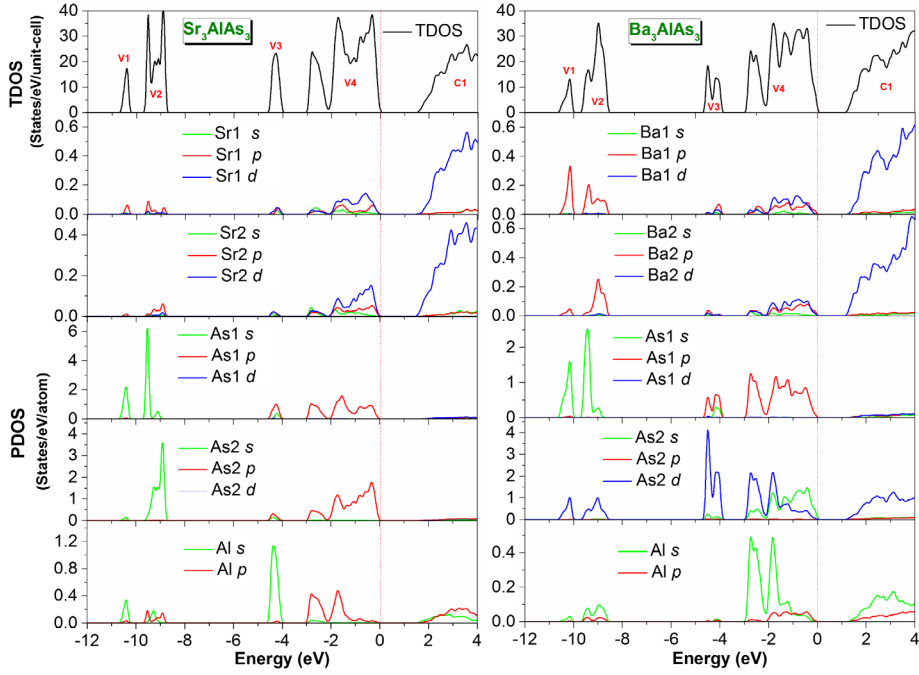
Figure 4. (colour online) Total and partial densities of states (TDOS and PDOS) diagrams for the Ae_3AlAs_3 (Ae = Sr, Ba) compounds.

contribution from an admixture of the Ba1-5p, Ba2-5p, As2-4d and Al-3s states. The second group V2, from −9.7 to −8.5 eV, is mainly formed of the As1-4s states with a small contribution from an admixture of the Ba1-5p, Ba2-5p, As2-4d and Al-3sp states. The third group V3, from −4.7 to −3.82 eV, is mainly composed of the As2-4d and As1-4p states with a small contribution from the Ba1-4p, Ba1-4d, Ba2-4p and Ba2-4d. The upper valence band group V4, from −3.05 eV up to Fermi level, is mainly due to the As1-4p and As2-4sd states with a small contribution from the Al-3p and Ba1-4pd orbitals. The bottom of the conduction band C1 is made up basically of the As2-4d, Ba1-4d and Ba2-4d states with a small contribution from the Al-3s and Al-3p states.

3.3.3. Effective mass

The effective mass of charge-carrier provides an opposite contribution to the Seebeck coefficient and electrical conductivity. A large effective mass of charge-carrier is favourable to improve the Seebeck coefficient; however, the high charge-carrier mobility requires a lighter effective mass. To further understand the electrical behaviour of the Ae_3AlAs_3 (Ae = Sr, Ba) compounds, it is necessary to estimate their effective masses of the charge-carries in various electron and hole pockets at the band edges. The effective mass of electrons (m_e^*) at the conduction band minimum (CBMi) and holes (m_h^*) at the valence band maximum (VBMa) can be evaluated through a simple parabolic fitting of the dispersion energy $E(k)$

Table 6. Calculated electron and hole effective masses (m_e^* and m_e^*, in units of free electron mass m_0) for the Sr_3AlAs_3 and Ba_3AlAs_3 compounds.

System	$m_e^*(\Gamma \rightarrow S)$	$m_e^*(\Gamma \rightarrow Y)$	$m_h^*(\Gamma \rightarrow S)$	$m_h^*(\Gamma \rightarrow Y)$
Sr_3AlAs_3	0.2007	0.2202	0.3225	4.0226
	$m_e^*(\Gamma \rightarrow S)$	$m_e^*(\Gamma \rightarrow Y)$	$m_h^*(Y \rightarrow T)$	$m_h^*(Y \rightarrow \Gamma)$
Ba_3AlAs_3	0.2158	0.3738	0.6161	0.5514

diagram: $E = \frac{\hbar k^2}{2m^*}$, where $\hbar$ is the Planck's constant, E is the band-edge energy as a function of the wave vector k and m^* is the effective mass. For Ba_3AlAs_3, the effective masses of the holes at the VBMa were calculated along the $Y \rightarrow T$ and $Y \rightarrow \Gamma$ directions and those of the electrons at the CBMi were evaluated along the $\Gamma \rightarrow S$ and $\Gamma \rightarrow Y$ directions. For Sr_3AlAs_3, the effectives masses of holes and electrons are calculated along the $\Gamma \rightarrow S$ and $\Gamma \rightarrow Y$ directions. The obtained results are listed in Table 6. From Table 6, it is clear that the electrons and holes effective masses show a relevant dependence on the k-direction in the two considered compounds, implying the anisotropy of this physical property. It is found also that the effective mass of electron at the conduction band minimum is small than that of the hole at the valence band maximum. Consequently, the p-type Ae_3AlAs_3 (Ae = Sr, Ba) compounds would have the highest Seebeck coefficient, while the n-type Ae_3AlAs_3 (Ae = Sr, Ba) compounds would have the largest electrical conductivity. In addition, we can predict that the charge-carrier mobility of the p-type Sr_3AlAs_3 (Ba_3AlAs_3) compound along the $\Gamma \rightarrow S$ ($\Gamma \rightarrow Y$) direction should be larger than that in the $\Gamma \rightarrow Y$ ($Y \rightarrow T$) direction.

3.4. Optical properties

The fundamental features of the linear response of a medium to the effect of an incoming electromagnetic radiation can be accessed from the knowledge of its complex dielectric function $\varepsilon(\omega)$, which is directly related to the interaction of photons with electrons. The imaginary part of the dielectric function $\varepsilon_2(\omega)$ ($\varepsilon_2(\omega) = Im\ \varepsilon(\omega)$; $\varepsilon(\omega) = \varepsilon_1(\omega) + j\varepsilon_2(\omega)$) is directly proportional to the intensity of optical absorption. In the framework of the linear-response theory, $\varepsilon_2(\omega)$ is calculated from the matrix elements of the electric dipole operator between the occupied states in the valence band and unoccupied states in the conduction band within the respect of the selection rules [58]. The real part of the dielectric function $\varepsilon_1(\omega)$ ($\varepsilon_1(\omega) = Re\ \varepsilon(\omega)$) can be assessed from the imaginary part $\varepsilon_2(\omega)$ via the Kramer–Kronig relationship [59]. All frequency dependent macroscopic optical functions, such as refractive index $n(\omega)$, absorption coefficient $\alpha(\omega)$, reflectivity $R(\omega)$ and electron energy-loss function $L(\omega)$, can be deduced from $\varepsilon_2(\omega)$ and $\varepsilon_1(\omega)$ using the well-known relationships [60,61]. Since the investigated compounds belong to the orthorhombic system, space group *Cmce*, it is necessary to calculate the three non-zero components of the dielectric tensor that correspond to the three polarisations of the electric field $\vec{E}$ of the incident electromagnetic

radiation along the three principal crystallographic directions: *a* ([100]), *b* ([010]) and *c* ([001]).

The calculated imaginary parts of the Sr_3AlAs_3 and Ba_3AlAs_3 dielectric functions for the three different polarisations, i.e. $\vec{E}//[100]$, $\vec{E}//[010]$ and $\vec{E}//[001]$, are presented in Figure 5(a). It is clear from Figure 5(a) that the optical properties of the considered compounds exhibit a noticeable anisotropy. To account for the features observed in the optical spectra, it is customary to consider transitions from occupied to unoccupied states in the electronic energy band structure, especially at the high symmetry points in the Brillouin zone. Our scrutiny of the $\varepsilon_2(\omega)$ curve of Sr_3AlAs_3 indicates that it rises speedily with practically the same rate for the three different polarisations of the incident radiation. The $\varepsilon_2(\omega)$ spectrum exhibits two peaks centred at approximately 3.99 and 4.56 eV when the incident radiation is polarised parallel to the [100] crystallographic direction, at 4.01 and 4.91 eV for $\vec{E}//[010]$ and at 4.53 and 4.97 eV when $\vec{E}//[001]$. Based on the calculated band structure and density of states diagrams, one can conclude that these peaks are mainly originated from the direct transitions between the Sr1-4*p* and Sr2-4*p* or As1-4*p* and As2-4*p* states in the valence band and the Sr-*3d* states in the conduction band. The absorptive part of the dielectric function of the single-crystal Ba_3AlAs_3 exhibits one peak centred at approximately 4.20 eV for $\vec{E}//[100]$, at 4.97 eV for $\vec{E}//[010]$ direction and at approximately 4.23 eV for $\vec{E}//[001]$. This peak is mainly due to the electronic direct transitions from the occupied state As1-4*p* or As2-4*s* to the unoccupied states Ba1-3*d* or Ba2-3*d*.
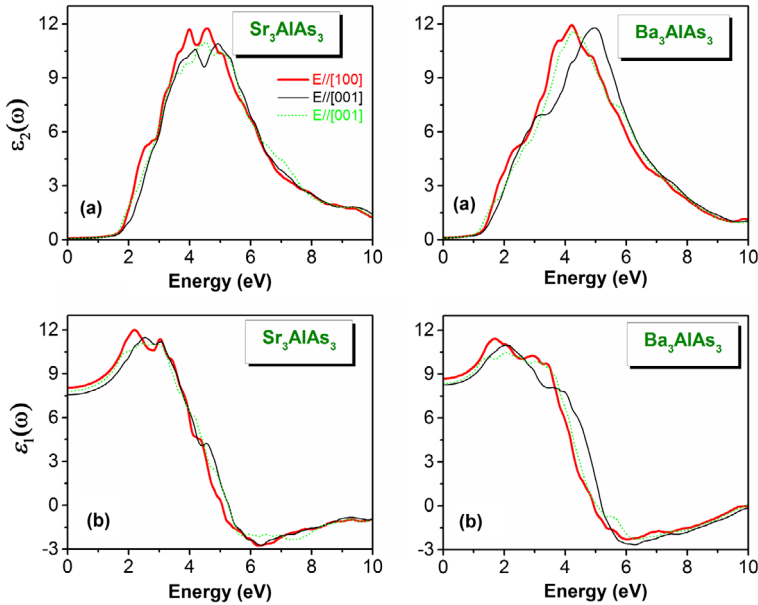

Figure 5. (colour online) Calculated imaginary ($\varepsilon_2(\omega)$) and real ($\varepsilon_1(\omega)$) parts of the dielectric function ($\varepsilon(\omega)$) as functions of photon energy for the Ae_3AlAs_3 (Ae = Sr, Ba) single-crystals for three different polarisations: $\vec{E}//[100]$, $\vec{E}//[010]$ and $\vec{E}//[001]$.

The dispersive parts ($\varepsilon_1(\omega)$) of the Sr_3AlAs_3 and Ba_3AlAs_3 dielectric functions are shown in Figure 5(b). The most important quantity in $\varepsilon_1(\omega)$ spectrum is the static dielectric constant, which is defined as the zero-energy value of the real part of the complex dielectric function: $\varepsilon_1(0) = \varepsilon_1(\omega \to 0)$. The $\varepsilon_1(0)$ is a parameter of fundamental importance in many aspects of material properties. Calculated $\varepsilon_1(0)$ value for Sr_3AlAs_3 (Ba_3AlAs_3) is found to be equal 8.048 (8.683) when $\vec{E}//[100]$, 7.566 (8.255) when $\vec{E}//[010]$ and 7.810 (8.361) when $\vec{E}//[001]$. One can note that the $\varepsilon_1(0)$ values corresponding to the three different polarisation directions are larger than the corresponding ones for Ba_3AlAs_3. This demonstrates that $\varepsilon_1(0)$ value is inversely proportional with the band gap; a smaller energy gap yields a larger $\varepsilon_1(0)$ value. This is consistent with the Penn's model [59] based on the expression $\varepsilon(0) \approx 1 + (h\omega_p/E_g)^2$.

The absorption coefficient $\alpha(\omega)$ describes the relative decrease in the incident radiation intensity when it passes through a medium. The calculated Sr_3AlAs_3 and Ba_3AlAs_3 absorption coefficients in a wider spectral region up to 15 eV for three different polarisations of the incident radiation: $\vec{E}//[100]$, $\vec{E}//[010]$ and $\vec{E}//[001]$ are displayed in Figure 6(a). The absorption edge in the Sr_3AlAs_3 compound starts at approximately 1.51 eV for the three different polarisations of the incident radiation. For the Ba_3AlAs_3 compound, the absorption edge begins approximately at 1.28 eV for the three different polarisations of the incident
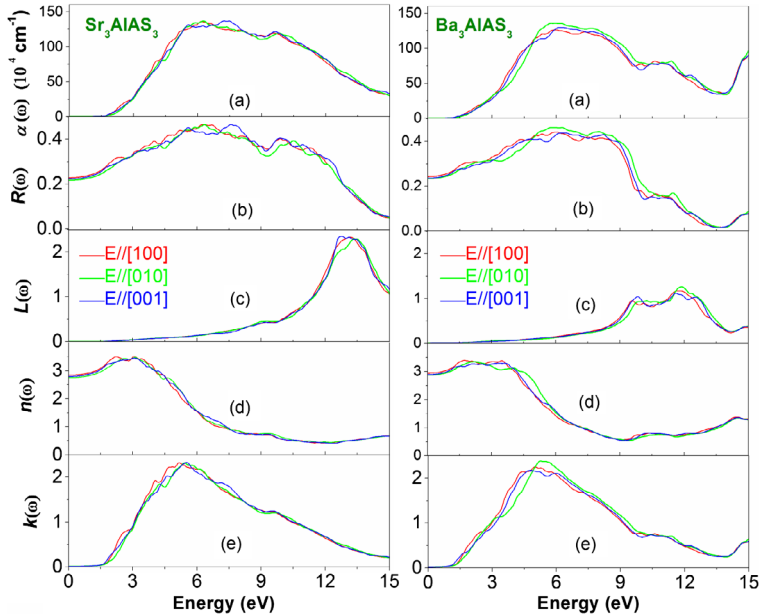
Figure 6. (colour online) Calculated optical function spectra: Absorption coefficient $\alpha(\omega)$, reflectivity $R(\omega)$, energy loss function $L(\omega)$, refractive index $n(\omega)$ and extinction coefficient $k(\omega)$ for the Sr_3AlAs_3 and Ba_3AlAs_3 single-crystals for three different polarisations: $\vec{E}//[100]$, $\vec{E}//[010]$ and $\vec{E}//[001]$.

radiation. A wide absorption band, located between 2 and 12 eV, characterises the considered compounds.

Figure 6(b) displays the calculated dependence of the reflectivity on the incident photon energy for three different polarisations for the Sr_3AlAs_3 and Ba_3AlAs_3 single-crystals. The zero frequency limit $R(0)$ of the Sr_3AlAs_3 (Ba_3AlAs_3) compound is equal to 23% (24%) for $\vec{E}//[100]$, 21% (23%) for $\vec{E}//[010]$ and 22% (23%) for $\vec{E}//[001]$. The reflectivity $R(\omega)$ enhances from $R(0)$ with increasing photon energy to acquire a maximum and then it decreases rapidly. From Figure 5(b), one can note that the maximum reflectivity in Sr_3AlAs_3 (Ba_3AlAs_3) arises approximately at 6.27 eV (6.00 eV) for $\vec{E}//[100]$, 6.35 eV (5.75 eV) for $\vec{E}//[010]$ and 7.60 eV (6.35 eV) for $\vec{E}//[001]$. This maximum attains 46% (44%) for $\vec{E}//[100]$, 46% (46%) for $\vec{E}//[010]$ and 43% (42%) for $\vec{E}//[001]$ in Sr_3AlAs_3 (Ba_3AlAs_3).

The energy-loss function $L(\omega)$ describes the energy-loss of a fast electron passing through a material [62]. The main peak of the $L(\omega)$ spectrum is generally defined as the bulk plasma frequency $(\omega)_p$, which occurs when $\varepsilon_2(\omega) < 1$ and $\varepsilon_1(\omega)$ reaches the zero point [63]. The plasma frequency for Sr_3AlAs_3 (Ba_3AlAs_3) is approximately equal to 13.15 eV (11.68 eV) for $\vec{E}//[100]$, 13.34 eV (11.87 eV) for $\vec{E}//[010]$ and 12.77 eV (11.60 eV) for $\vec{E}//[001]$ (Figure 6(c)). When the frequency of incident light is higher than the plasma frequency, the material becomes transparent, and hence an abrupt reduction of the reflectivity occurs at the corresponding energy.

The refractive index $n(\omega)$ of a material describes the difference between the propagation of an electromagnetic wave through vacuum and in a material. The extinction coefficient directly describes the attenuation of the electromagnetic waves in a material, and it is also known as a damping constant attenuation coefficient. The knowledge of the refractive index of an optical compound is important for its use in optical devices, such as photonic crystals and waveguides. Figure 6(d) shows the refractive index of Sr_3AlAs_3 and Ba_3AlAs_3 in relation with the energy of incident radiation. It is found that the static refractive index $n(0)$ (the value of refraction index at zero energy) for Sr_3AlAs_3 (Ba_3AlAs_3) compound is 2.83 (2.94) for $\vec{E}//[100]$, 2.75 (2.87) for $\vec{E}//[010]$ and 2.79 (2.89) for $\vec{E}//[100]$.

Static optical anisotropy for the title compounds can be quantified by an anisotropy rate, which can be expressed as follows [64,65]:

$$A_{OPT} = \left[\frac{\varepsilon_1(0)^{[direction]}}{\varepsilon_1(0)^{[polycristalline]}}, \frac{n(0)^{[direction]}}{n(0)^{[polycristalline]}} \right]$$

Here, $\varepsilon_1(0)^{[direction]}$ ($n(0)^{[direction]}$) is the value of $\varepsilon_1(0)$ ($n(0)$) along principal optical axes and $\varepsilon_1(0)^{[polycristalline]}$ ($n(0)^{[polycristalline]}$) is its value in polycrystalline. A material is optically isotropic if $A_{OPT} = 1$; otherwise, it is optically anisotropic. The degree of deviation of A_{OPT} from unity reveal the extent of the optical anisotropy. The calculated values of A_{OPT} are shown in Table 7. The calculated A_{OPT} values

Table 7. Calculated static dielectric constants $\varepsilon_1(0)$, static refractive indexes $n(0)$ and optical anisotropy A_{OPT} for the Sr_3AlAs_3 and Ba_3AlAs_3 compounds in polycrystalline and along the principal optical axes:[100], [010] and [001].

| System		$\varepsilon_1(0)$	$n(0)$	A_{OPT}
Sr_3AlAs_3	Polycrystalline	7.808	2.79	
	[100]	8.048	2.82	[1.031, 1.011]
	[010]	7.566	2.75	[0.969, 0.986]
	[001]	7.810	2.79	[1.0, 1.0]
Ba_3AlAs_3	Polycrystalline	8.433	2.90	
	[100]	8.683	2.94	[1.030, 1.014]
	[010]	8.255	2.87	[0.979, 0.990]
	[001]	8.361	2.89	[0.991, 0.997]

reveal that the two studied compounds exhibit a certain optical anisotropy. The maximum optical anisotropy occurs along the [010] crystallographic direction.

3.5. Thermoelectric properties

When two dissimilar points of a thermoelectric material are held at different temperatures, a voltage of several microvolts per Kelvin between these two points arises. An efficient thermoelectric material should possess high Seebeck coefficient (S) (in order to convert maximum heat to electrical power) and high electrical conductivity σ while keeping the thermal conductivity κ low as much as possible. So, in order to study the thermoelectric properties of the orthorhombic Ae_3AlAs_3 (Ae = Sr, Ba) compounds, we have calculated the basic transport parameters, e.g. Seebeck coefficient (S, in µVK^{-1}), electrical conductivity scaled by relaxation time (σ/τ, in $\Omega^{-1}m^{-1}s^{-1}$), thermal conductivity scaled by relaxation time (κ/τ, in WK^{-1} m^{-1}s^{-1}), power-factor ($PF = S^2 s/\tau$, in WK^{-2}m^{-1}s^{-1}) and factor of merit ($ZT = \sigma S^2 T/\kappa$, dimensionless), as function of both charge-carrier concentration and temperature. The thermoelectric properties of the examined compounds were calculated for temperature between 300 and 900 K and for charge-carrier concentration between 1×10^{18} and 1×10^{21}cm^{-3}, which is an optimum charge-carrier concentration range for better thermoelectric performance, using the semi classical Boltzmann theory as implanted in the BoltzTraP computer package [66] with a dense k-mesh of $50 \times 50 \times 50$. As the investigated compounds crystalise in an orthorhombic system, we have first investigated the directional dependence of the thermoelectrical parameters. We find that the two considered compounds exhibit almost isotropic behaviour in the TE parameters along the three principal crystallographic directions. Since there is no significant anisotropy observed in the TE parameters, we have presented only their average values.

Figure 7 shows the variation of the Seebeck coefficient S (thermopower), electrical conductivity scaled by relaxation time σ/τ, electronic thermal conductivity scaled by relaxation time κ/τ and power-factor PF with charge-carrier concentration for both n-type and p-type Sr_3AlAs_3 and Ba_3AlAs_3 compounds at 300, 600 and 900 K. Panel (a) of Figure 6 demonstrates that the absolute value (magnitude)
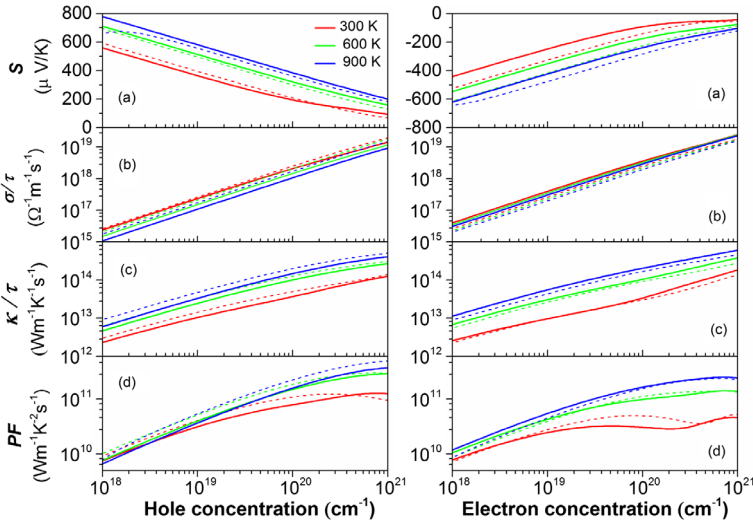
Figure 7. (colour online) Calculated average Seebeck coefficient (*S*; panel a), electrical conductivity scaled by relaxation time (σ/τ; panel b), thermal conductivity scaled by relaxation time (κ/τ; panel c) and power-factor ($PF = S^2\sigma/\tau$ panel d) as functions of both electron and hole concentrations at 300, 600 and 900 K for the Sr$_3$AlAs$_3$ (solid lines) and Ba$_3$AlAs$_3$ (dotted lines) compounds.

of *S* decreases with an increasing charge-carrier concentration for both *n*-type and *p*-type doping at a fixed temperature. The magnitude of *S* increases with an increasing temperature due to the increase of charge-carrier concentration for both charge-carrier types; this is a common trend in thermoelectric materials. One can note that the considered compounds possess larger thermopower for the holes compared with the electrons throughout the considered temperature range. For the same carrier concentration, the difference in Seebeck coefficient between electrons and holes is of the order of 200 μV/K. This result is consistent with the calculated charge-carrier masses; large Seebeck coefficient translates to large effective masses of charge-carries. The thermopower shows practically the same behaviour regarding the variation of charge-carrier concentration and temperature for the two title compounds. This comportment is might be due to the similarity of their band dispersions around the Fermi level and their effective masses, which are close to each other. For the same concentration and same type of charge-carrier, the two studied compounds have almost equal value for the thermopower at the same fixed temperature. To have an idea about the thermopower efficiency of the title compounds, we have compared their Seebeck coefficient *S* with a traditional thermoelectric material, Bi$_2$Te$_3$. It was reported that at 300 K and charge-carrier concentration of 4×10^{18} cm^{-3}, Bi$_2$Te$_3$ has a thermopower of 313 μVK^{-1} for *p*-doping and of 196 μVK^{-1} for *n*-doping [67,68], while our investigated compound Sr$_3$AlAs$_3$ (Ba$_3$AlAs$_3$), at the same conditions, has a Seebeck coefficient *S* equal to approximately 442 (472) μVK^{-1} for *p*-doping and −327 (−404) μVK^{-1} for *n*-doping. From this, one can appreciate that the thermopower value of the examined materials is larger than that of the traditional thermoelectric compound. This allows
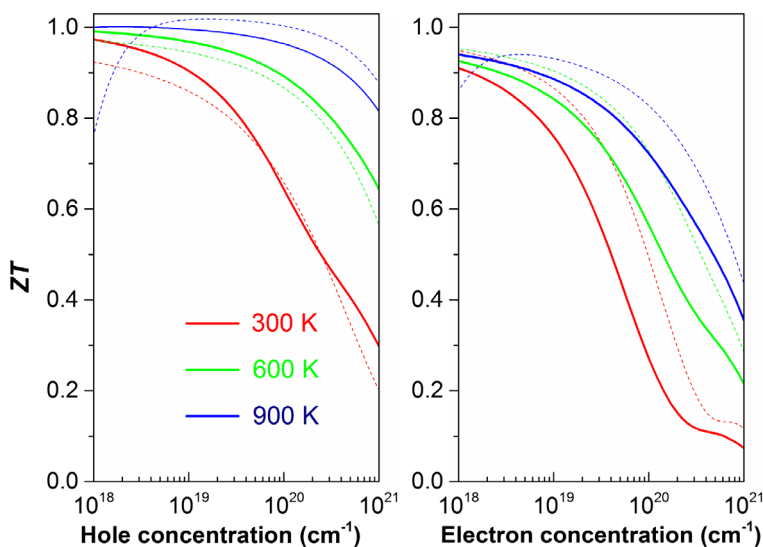
Figure 8. (colour online) Calculated figure of merit ZT as a function of charge-carrier concentration of both electron and hole concentrations at 300, 600 and 900 K for the Sr_3AlAs_3 (solid lines) and Ba_3AlAs_3 (dotted lines) compounds.

us to claim that the Sr_3AlAs_3 and Ba_3AlAs_3 systems are potential candidates for thermoelectric applications if one can more reduce their thermal conductivity by some techniques, such as alloying, nano-structuring or superlattice growth.

Panels (b) and (c) of Figure 7 demonstrate that the electrical and thermal conductivities scaled by relaxation time (σ/τ and κ/τ) increase with an increasing charge-carrier concentration in the two considered compounds for both n-type and p-type doping at a fixed temperature. It is found that the σ/τ value of the electrons is larger than that of the holes.

Figure 8 depicts the variation of the figure of merit (ZT) as function of hole and electron concentrations at 300, 600 and 900 K for Sr_3AlAs_3 and Ba_3AlAs_3. One can note that at the same temperature and same charge-carrier concentration, the maximum figure of merit (ZT) is found in the hole-doped systems. At 900 K, the ZT is equal 1.02 (1.00) in the p-doped Sr_3AlAs_3 (Ba_3AlAs_3) and 0.93 (0.89) in the n-doped Sr_3AlAs_3 (Ba_3AlAs_3).

4. Conclusion

In summary, we have investigated in detail the structural, electronic, optical and thermoelectric properties of the new ternary arsenides Ae_3AlAs_3 (Ae = Sr, Ba) using first principles calculations.

Our main findings are as follows:

(i) The calculated structural parameters agree very well with the available experimental findings.

(ii) The two examined compounds are mechanically stable and exhibit a noticeable elastic anisotropy. Sr_3AlAs_3 (Ba_3AlAs_3) will behave as brittle (ductile) with rather moderate stiffness.

(iii) The calculated band structures using the TB-mBJ potential reveal that Sr_3AlAs_3 and Ba_3AlAs_3 are semiconductors with band gaps equal to 1.51 and 1.28 eV, respectively.

(iv) The calculated dielectric function, extinction coefficient, reflective index, reflectivity and electron energy-loss function for polarised incident radiation along the principal crystallographic directions show noticeable anisotropy. The origin of the features that appear in the optical spectra has discussed. The static dielectric constants $\varepsilon(0)$, refractive index $n(0)$ and plasmon energy were estimated.

(v) We found that Sr_3AlAs_3 and Ba_3AlAs_3 are promising TE materials with a high Seebeck coefficient and electrical conductivity, but their figures of merit are limited by their large thermal conductivity.

Acknowledgement

Disclosure statement

No potential conflict of interest was reported by the authors.

Funding

ORCID

Y. Al-Douri http://orcid.org/0000-0002-5175-6372

References

[1] G.J. Snyder and E.S. Toberer, *Complex thermoelectric materials*, Nat. Mater. 7 (2008), pp. 105–114.

[2] A.I. Hochbaum, R. Chen, R.D. Delgado, W. Liang, E.C. Garnett, M. Najarian, A. Majumdar, and P. Yang, *Enhanced thermoelectric performance of rough silicon nanowires*, Nature 451 (2008), pp. 163–167.

[3] Y. Pei, A.D. LaLonde, N.A. Heinz, X. Shi, S. Iwanaga, H. Wang, L. Chen, and G.J. Snyder, *Stabilizing the optimal carrier concentration for high thermoelectric efficiency*, Adv. Mater. 23 (2011), pp. 5674–5678.

[4] S.M. Kauzlarich, S.R. Brown, and G.J. Snyder, *Zintl phases for thermoelectric devices*, Dalton Trans. 133 (2007), pp. 2099–2107.

[5] G. Chen, M.S. Dresselhaus, G.J.P. Fleurial, and T. Caillat, *Recent developments in thermoelectric materials*, Int. Mater. Rev. 48 (2003), pp. 45–66.

[6] M.S. Dresselhaus, G. Chen, M.Y. Tang, R.G. Yang, H. Lee, D.Z. Wang, Z.F. Ren, J.P. Fleurial, and P. Gogna, *New directions for low-dimensional thermoelectric materials*, Adv. Mater. 19 (2007), pp. 1043–1053.

[7] C. Uher, *Skutterudites: Prospective Novel Thermoelectrics*, in *Recent Trends in Thermoelectric Materials Research I, Semimetals and Semimetals Series*, Terry M. Tritt, eds., Vol. 69, Elsevier, Amsterdam, 2001, pp. 139–253.

[8] G.S. Nolas, J. Poon, and M. Kanatzidis, Recent developments in bulk thermoelectric materials, MRS Bull. 31 (2006), pp. 199–205.

[9] G.J. Snyder, M. Christensen, E. Nishibori, T. Caillat, and B.B. Iversen, *Disordered zinc in Zn4Sb3 with phonon-glass and electron-crystal thermoelectric properties*, Nat. Mater. 3 (2004), pp. 458–463.

[10] F. Casper, T. Graf, S. Chadov, B. Balke, and C. Felser, Half-Heusler compounds: Novel materials for energy and spintronic applications, Semicond. Sci. Technol. 27 (2012), p. 063001.

[11] K. Koumoto, Y. Wang, R. Zhang, A. Kosuga, and R. Funahashi, Oxide thermoelectric materials: A nanostructuring approach, Annu. Rev. Mater. Res. 40 (2010), pp. 363–394.

[12] K. Koumoto, I. Terasaki, and R. Funahashi, *Complex oxide materials for potential thermoelectric applications*, MRS Bull. 31 (2006), pp. 206–210.

[13] S.M. Kauzlarich (ed.), *Chemistry, Structure and Bonding of Zintl Phases and Ions, Selected Topics and Recent Advances*, John Wiley-VCH, Weinheim, 1996.

[14] E.S. Toberer, A.F. May, and G.J. Snyder, *Zintl chemistry for designing high efficiency thermoelectric materials*, Chem. Mater. 22 (2010), pp. 624–634.

[15] E.S. Toberer, A. Zevalkink, N. Crisosto, and G.J. Snyder, The Zintl compound Ca5Al2Sb6 for low-cost thermoelectric power generation, Adv. Funct. Mater. 20 (2010), pp. 4375–4380.

[16] E.S. Toberer, C.A. Cox, S.R. Brown, T. Ikeda, A.F. May, S.M. Kauzlarich, and G.J. Snyder, *Traversing the metal-insulator transition in a Zintl phase: Rational enhancement of thermoelectric efficiency in Yb14Mn1−xAlxSb11*, Adv. Funct. Mater. 18 (2008), pp. 2795–2800.

[17] A. Zevalkink, G. Pomrehn, Y. Takagiwa, J. Swallow, and G.J. Snyder, *Thermoelectric properties and electronic structure of the Zintl-phase Sr3AlSb3*, ChemSusChem. 6 (2013), pp. 2316–2321.

[18] G.J. Snyder and E.S. Toberer, *Complex thermoelectric materials*, Nat. Mater. 7 (2008), pp. 105–114.

[19] Y. Pei, A.D. LaLonde, N.A. Heinz, X. Shi, S. Iwanaga, H. Wang, L. Chen, and G.J. Snyder, Stabilizing the optimal carrier concentration for high thermoelectric efficiency, Adv. Mater. 23 (2011), pp. 5674–5678.

[20] A. Zevalkink, E.S. Toberer, W.G. Zeier, E. Flage-Larsen, and G.J. Snyder, *Ca3AlSb3: An inexpensive, non-toxic thermoelectric material for waste heat recovery*, Energy Environ. Sci. 4 (2011), pp. 510–518.

[21] Y.L. Yan and Y.X. Wang, *Crystal structure, electronic structure, and thermoelectric properties of Ca5Al2Sb6*, J. Mater. Chem. 21 (2011), pp. 12497–12502.

[22] J.P. Perdew and A. Zunger, *Self-interaction correction to density-functional approximations for many-electron systems*, Phys. Rev. B 23 (1981), pp. 5048–5079.

[23] S.S. Stoyko, L.H. Voss, H. He, and S. Bobev, Synthesis, crystal and electronic structures of the pnictides AE3TrPn3 (AE = Sr, Ba; Tr = Al, Ga; Pn = P, As), Crystals 5 (2015), pp. 433–446.

[24] S.J. Clark, M.D. Segall, C.J. Pickard, P.J. Hasnip, M.J. Probert, K. Refson, and M.C. Payne, *First principles methods using CASTEP*, Z. Kristallogr. 220 (2005), pp. 567–570.

[25] P. Blaha, K. Schwarz, G.K.H. Madsen, D. Kvasnicka, and J. Luitz, *WIEN2k: An Augmented plane wave plus local orbitals program for calculating crystal properties*, Vienna University of Technology, Vienna, 2001.

[26] D. Vanderbilt, *Soft self-consistent pseudopotentials in a generalized eigenvalue formalism*, Phys. Rev. B. 41 (1990), pp. 7892–7895.

[27] J.P. Perdew, A. Ruzsinszky, G.I. Csonka, O.A. Vydrov, G.E. Scuseria, L.A. Constantin, X.L. Zhou, and K. Burke, Restoring the density-gradient expansion for exchange in solids and surfaces, Phys. Rev. Lett. 100 (2008), p. 136406.

[28] H.J. Monkhorst and J.D. Pack, Special points for Brillouin-zone integrations, Phys. Rev. B. 13 (1976), pp. 5188–5192.

[29] P. Dufek, P. Blaha, and K. Schwarz, *Applications of Engel and Vosko's generalized gradient approximation in solids*, Phys. Rev. B 50 (1994), pp. 7279–7283.

[30] E. Engel and S.H. Vosko, *Exact exchange-only potentials and the virial relation as microscopic criteria for generalized gradient approximations*, Phys. Rev. B 47 (1993), pp. 13164–13174.

[31] X. Zhu, S. Fahy, K.J. Chang, and S.G. Louis, *Ab initio calculation of pressure coefficients of band gaps of silicon: Comparison of the local-density approximation and quasiparticle results*, Phys. Rev. B 39 (1989), pp. 7840–7847.

[32] P.P. Rushton, D.J. Tozer, and S.J. Clark, *Nonlocal density-functional description of exchange and correlation in silicon*, Phys. Rev. B. 65 (2002), p. B864.

[33] B. Králik, E.K. Chang, and S.G. Louie, *Structural properties and quasiparticle band structure of zirconia*, Phys. Rev. B 57 (1998), pp. 7027–7036.

[34] F. Tran and P. Blaha, Accurate band gaps of semiconductors and insulators with a semilocal exchange-correlation potential, Phys. Rev. Lett. 102 (2009), p. 226401.

[35] P.E. Blöchl, O. Jepsen, and O. K. Andersen, *Improved tetrahedron method for Brillouin-zone integrations*, Phys. Rev. B 49 (1994), pp. 16223–16233.

[36] C.A. Ponce, R.A. Casali, M.A. Caravaca, *Ab initio study of mechanical and thermo-acoustic properties of tough ceramics: Applications to HfO$_2$ in its cubic and orthorhombic phase*. J. Phys.: Condens. Mater. 20 (2008), p. 045213.

[37] A. Bouhemadou, R. Khenata, M. Chegaar, and S. Maabed, *First-principles calculations of structural, elastic, electronic and optical properties of the antiperovskite AsNMg3*, Phys. Lett. A 371 (2007), pp. 337–343.

[38] D.C. Wallace, *Thermodynamics of Crystals*, John Wiley, New York, NY, 1972.

[39] R. Hill, *The elastic behaviour of a crystalline aggregate*, Proc. Phys. Soc. Lond. A. 65 (1952), pp. 349–354.

[40] W. Voigt, *Lehrbuch der Kristallphysik*, Taubner, Leipzig, 1928.

[41] A. Reuss, *Berechnung der fließgrenze von mischkristallen auf grund der plastizitätsbedingung fur Einkristalle*, Zeitschrift Angew. Math. Mech. 9 (1929), pp. 49–58.

[42] A. Bedjaoui, A. Bouhemadou, S. Aloumi, R. Khenata, S. Bin-Omran, Y. Al-Douri, F. Saad Saoud, and S. Bensalem, *Structural, elastic, electronic and optical properties of the novel quaternary diamond-like semiconductors Cu2MgSiS4 and Cu2MgGeS4*, Solid State Sci. 70 (2017), pp. 21–35.

[43] E. Schreiber, O.L. Anderson, and N. Soga, *Elastic Constants and Their Measurements*, McGraw-Hill, New York, NY, 1973.

[44] J.W. Soh, H.M. Lee, and H.-S. Kwon, Relation between Poisson's ratio and ionicity in simple binary cubic compounds, J. Alloys Compd. 194 (1993), pp. 119–125.

[45] S.F. Pugh, *Relations between the Elastic Moduli and the plastic properties of polycrystalline pure metals*, Phil. Mag. 45 (1954), pp. 823–843.

[46] S. Chen, Y. Sun, Y.-H. Duan, B. Huang, and M.-J. Peng, Phase stability, structural and elastic properties of C15-type Laves transition-metal compounds MCo2 from first-principles calculations, J. Alloys Compd. 630 (2015), pp. 202–208.

[47] D.G. Pettifor, *Theoretical predictions of structure and related properties of intermetallics*, Mater. Sci. Technol. 8 (1992), pp. 345–349.

[48] P. Jund, R. Viennois, X. Tao, K. Niedziolka, and J.C. Tédenac, *Physical properties of thermoelectric zinc antimonide using first-principles calculations*, Phys. Rev. B 85 (2012), p. 423.

[49] A.L. Anderson, A simplified method for calculating the debye temperature from elastic constants, J. Phys. Chem. Solids 24 (1963), pp. 909–917.

[50] V. Tvergaard and J.W. Hutchinson, *Microcracking in ceramics induced by thermal expansion anisotropy*, J. Am. Ceram. Soc. 71 (1988), pp. 157–166.

[51] B. Xiao, J. Feng, C.T. Zhou, Y.H. Jiang, and R. Zhou, *Mechanical properties and chemical bonding characteristics of Cr7C3 type multicomponent carbides*, J. Appl. Phys. 109 (2011), p. 023507.

[52] K. Lau and A.K. McCurdy, *Elastic anisotropy factors in orthorhombic, tetragonal, and hexagonal Crystals*, Phys. Rev. B. 58 (1998), pp. 8980–8984.

[53] P. Ravindran, L. Fast, P.A. Korzhavyi, and B. Johansson, *Density functional theory for calculation of elastic properties of orthorhombic crystals: Application to TiSi2*, J. Appl. Phys. 84 (1998), pp. 4891–4904.

[54] D.H. Chung and W.R. Buessem, *The Elastic Anisotropy of Crystals*, in *Proceeding of International Symposium 2*, F.W. Vahldiek and S.A. Mersol, eds., Plenum Press, New York, NY, 1968, pp. 217–245.

[55] K.B. Panda and K.S.R. Chandran, *Determination of elastic constants of titanium diboride (TiB2) from first principles using FLAPW implementation of the density functional theory*, Comput. Mater. Sci. 35 (2006), pp. 134–150.

[56] S. Ranganathan and M. Ostoja-Starzewski, *Universal elastic anisotropy index*, Phys. Rev. Lett. 101 (2008), p. 055504.

[57] J.F. Nye, *Physical Properties of Crystals: Their Representation by Tensors and Matrices*, Oxford University Press, Great Britain, 1957.

[58] F. Wooten, *Optical Proprieties of Solid*, Academic, New York, NY, 1972.

[59] M. Alouani and J.M. Wills, *Calculated optical properties of Si, Ge, and GaAs under hydrostatic pressure*, Phys. Rev. B 54 (1996), pp. 2480–2490.

[60] M. Fox, *Optical Properties of Solids*, Oxford University Press, New York, NY, 2001.

[61] M. Dressel and G. Gruner, *Electrodynamics of solids: Optical properties of electrons in matter*, Cambridge University Press, Cambridge, 2002.

[62] A. Bouhemadou and R. Khenata, *Ab initio study of the structural, elastic, electronic and optical properties of the antiperovskite SbNMg3*, Comput. Mater. Sci. 39 (2007), pp. 803–807.

[63] R. Saniz, L.H. Ye, T. Shishidou, and A.J. Freeman, *Structural, electronic, and optical properties of NiAl$_3$: first-principles calculations*, Phys. Rev. B. 74 (2006), pp. 014209.

[64] D. Yonghua, M. Lishi, L. Ping, and C. Yong, *First-principles calculations of electronic structures and optical, phononic, and thermodynamic properties of monoclinic α-spodumene*, Ceram. Internat. 43 (2017), pp. 6312–6321.

[65] D. Cherrad, D. Maouche, M. Boudissa, M. Reffas, L. Louail, M. Maamache, K. Haddadi, and Y. Medkour, *Ultra soft pseudo potential investigation of fundamental physical properties*

of CaXO3 (X=Sn and Hf) distorted perovskites: A reference study to the perfect perovskites, Physica B 429 (2013), pp. 95–105.

[66] G.K.H. Madsen and D.J.S. Singh, BoltzTraP. A code for calculating band-structure dependent quantities, Comput. Phys. Commun. 175 (2006), pp. 67–71.

[67] P.C. Sreeparvathy, V. Kanchana, and G. Vaitheeswaran, *Thermoelectric properties of zinc based pnictide semiconductors*, J. App. Phys. 119 (2016), p. 085701.

[68] T.J. Scheidemantel, C. Ambrosch-Draxl, T. Thonhauser, J.V. Badding, and J.O. Sofo, *Transport coefficients from first-principles calculations*, Phys. Rev. B 68 (2003), p. 331.